aerospace

MDPI

Article

Characterization of the Endwall Flow in a Low-Pressure Turbine Cascade Perturbed by Periodically Incoming Wakes, Part 1: Flow Field Investigations with Phase-Locked Particle Image Velocimetry

Tobias Schubert, Dragan Kožulović and Martin Bitter *

Institute of Jet Propulsion, University of the Bundeswehr Munich, Werner-Heisenberg-Weg 39, 85577 Neubiberg, Germany
* Correspondence: martin.bitter@unibw.de

Abstract: Particle image velocimetry (PIV) measurements were performed inside a low-pressure turbine cascade operating at engine-relevant high-speed and low-Re conditions to investigate the near-endwall flow. Of particular research interest was the dominant periodic disturbance of the flow field by incoming wakes, which were generated by moving cylindrical bars at a frequency of 500 Hz. Two PIV setups were utilized to resolve both (1) a large blade-to-blade plane close to the endwall as well as midspan and (2) the wake effects in an axial flow field downstream of the blade passage. The measurements were performed using a phase-locked approach in order to align and compare the results with comprehensive CFD data that are also available for this test case. The experimental results not only support a better understanding and even a quantification of the wake-induced over/under-turning inside and downstream of the passage, they also enable the tracing of the 'negative-jet-effect', which is widely known in the CFD branch of the turbomachinery community but is seldom visualized in experiments. The results also reveal that the bar wake periodically widens the blade wake by up to 165%, while the secondary flow is less affected and exhibits a phase lag with respect to the 2D-flow effects. The results presented here are an essential basis for the subsequent investigation of the near-endwall blade suction surface effects using unsteady pressure-sensitive paint in the second part of this two-part publication.

Keywords: rotor–stator interaction; negative jet; passage flow field; phase-locked particle image velocimetry (PIV)

Citation: Schubert, T.; Kožulović, D.; Bitter, M. Characterization of the Endwall Flow in a Low-Pressure Turbine Cascade Perturbed by Periodically Incoming Wakes, Part 1: Flow Field Investigations with Phase-Locked Particle Image Velocimetry. *Aerospace* **2024**, *11*, 403. https://doi.org/10.3390/aerospace11050403

Academic Editor: Lin Chen

Received: 14 March 2024
Revised: 25 April 2024
Accepted: 3 May 2024
Published: 16 May 2024

1. Introduction

The establishment of high-lift blade designs in modern jet engines and the ongoing trend to reduce weight by lowering the solidity in low-pressure turbine (LPT) vanes has triggered a lot of research on endwall flow in recent years. The main motivation is the significant contribution to overall losses due to high pressure gradients in the blade passage and thus intensified endwall flow. In the case of low-aspect-ratio LPT blades, for which a larger range of the blade span is affected, the endwall losses are approximated to account for one third of the overall losses, see [1]. Based on a numerical parametric design study in LPT cascades, Coull [2] found that endwall losses can be decomposed into two major components: dissipation in the endwall boundary layer and induced losses by secondary flows, which scale with streamwise vorticity. According to Denton and Pullan [3], the secondary flow itself exhibits several sources of loss, such as flow interactions inside the blade passage and downstream mixing losses. Particularly, the interaction of the passage vortex and the blade suction surface, resulting in the counter rotating vortex, was found to have a strong contribution to the overall losses by Cui and Tucker [1] as well as Bear et al. [4]. The endwall flow development is also largely dependent on the inflow

conditions. The effects of periodically incoming wakes were investigated in the T106A and T106Div turbine cascades using measurements and numerical simulations (CFD) by Ciorciari et al. [5,6]. Both approaches have shown an attenuation of the secondary flow. In contrast to the relatively small effects of incoming wakes, Volino et al. [7] found the influence of the inlet boundary layer to be much larger. Schubert and Niehuis [8] came to a similar conclusion when evaluating the turbine cascade exit flow; however, they found that the endwall flow development inside the blade passage is significantly affected by both factors, but in different manners. The vast majority of research dealing with secondary flow investigations has been centered around probe-based measurements: mostly up- and downstream of the blade passage. More recently, some published works have diverged from this classic approach by incorporating more modern experimental methods. For example, Sinkwitz et al. [9] and Lopez et al. [10] utilized hot-film sensor arrays on the near-endwall suction surface, and Chemnitz and Niehuis [11] analyzed the potential of particle image velocimetry (PIV) in comparison to five-hole-probe (FHP) and constant temperature anemometry (CTA) measurements in turbine cascade exit flow.

Despite the vast research activity in recent years, the accurate prediction and reduction of endwall loss is expected to remain a challenge for many years to come [3]. Aimed at providing a further step in the continued understanding of endwall flow and its determining factors, an extensive research program funded by the Deutsche Forschungsgemeinschaft (DFG) was launched in 2018 by four German university institutes, see Engelmann et al. [12]. Within this conglomerate, the Institute of Jet Propulsion of the University of the Bundeswehr Munich covered low-pressure turbine aspects at high-speed flow conditions. This paper is based on the design work and first experimental and CFD results by Schubert et al. [8,13]. They used a particular turbine cascade design to investigate the effects of boundary layer conditions and periodically incoming wakes on the secondary flows and losses. The subsequent goal was to validate, complement, and specify the previous findings by conducting state-of-the-art optical measurements inside the blade passage, which poses a far greater challenge in terms of experimental setup. Thereby, the present work will demonstrate how the classic approach to secondary flow investigations can be extended and enhanced to form a more comprehensive picture. The discussion of PIV results shall be the focus of part one of this two-part publication, while the second part will present unsteady pressure-sensitive paint (i-PSP) measurements.

2. Methods

2.1. Test Case

The presented experiments were conducted using a linear cascade of the T106A low-pressure turbine profile. The key geometric and flow parameters are summarized in Table 1. The T106 cascade has a long research history, and the aerodynamic performance of the original design is well known under various operating conditions, see, e.g., Kampitsch et al. [14], Kirik and Niehuis [15], or Michelassi et al. [16]. However, the cascade used here is a redesign that was specifically developed for endwall flow measurements under periodic inflow and high-speed conditions ($M_{2th} = 0.59$, $Re_{2th} = 2 \times 10^5$). The blade profile geometry remains unchanged, though. The main features of the current cascade are a sufficiently thick endwall boundary layer and the ability to perform variations in the boundary layer conditions on this endwall. The challenge regarding the endwall boundary layer stems from a gap between the wind tunnel and the cascade endwalls upstream of the blade passages. This gap, which is needed for the moving bar wake generator, enables a leakage flow driven by a negative pressure gradient. While the freestream flow is not affected, it can act as a boundary layer suction, leading to weak secondary flow. To counteract this problem, the current cascade features an integrated split flat plate at part-span that serves as a turbine endwall (marked in yellow in Figure 1). Using a modular composition of the aft plate, various measurement techniques can be implemented with manageable effort. The endwall boundary layer can be adjusted by misaligning the front plate with respect to the aft plate. During all measurements presented in this paper, the

endwall boundary layer thickness was δ_{99} = 4.62 mm with a shape factor of H_{12} = 1.86 at 45% Chord C upstream of the blade's leading edge (LE). A detailed description of the particular test case design and an investigation of the effects of endwall boundary layer variations on the secondary flow and loss production can be found in [8,13].

Table 1. T106A linear turbine cascade.

Geometric parameters:	
Chord length C	100 mm
Pitch-to-chord ratio P/C	0.799
Aspect ratio H/C	1.31
Flow conditions:	
Exit Mach number M_{2th}	0.59
Exit Reynolds number Re_{2th}	2×10^5
Design inflow angle β_1	127.7°
Design outflow angle β_2	26.8°
Turbulence intensity Tu_1	6.8%
Periodically unsteady inflow conditions:	
Strouhal number Sr	0.66
Flow coefficient ϕ	3.8

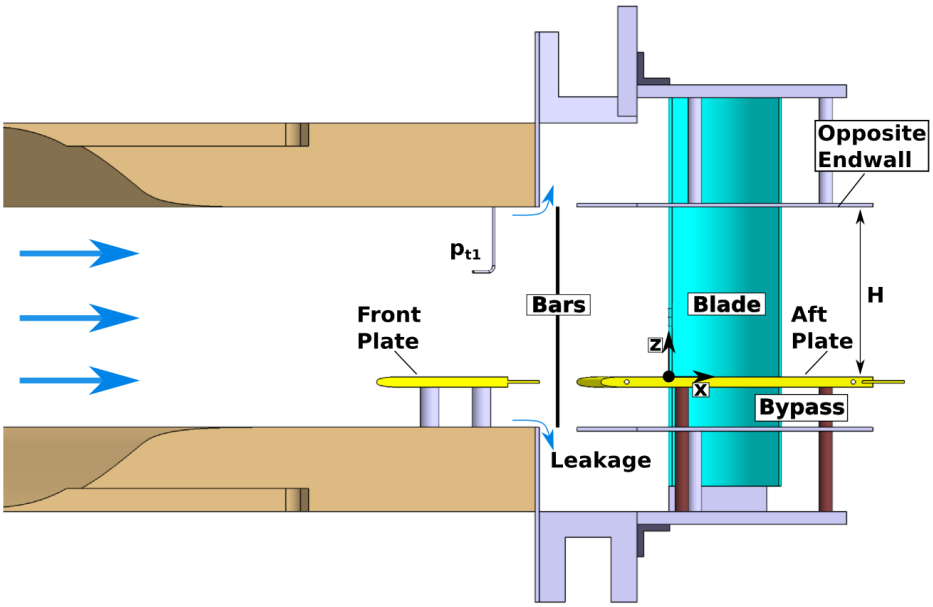

Figure 1. Illustration of the T106A test case featuring a split flat plate endwall (yellow) and moving bars upstream of the low-pressure turbine blades (cyan); adapted from Schubert et al. [8].

2.2. Numerical Setup

Numerical simulations were utilized during the cascade design (pre-test CFD) as well as to support the experimental results (validated post-test CFD) with time-resolved flow data, especially in areas of limited accessibility. The unsteady simulations were performed using the (U)RANS flow solver TRACE by DLR with the $k-\omega$ turbulence model by Wilcox [17] and $\gamma Re_{\theta t}$ transition model by Langtry and Menter [18]. The computational domain covers a single blade pitch with periodic boundary conditions. It is divided into an upstream block group encompassing the front plate, a moving domain containing two bar pitches, and a downstream block group that encompasses the blade passage and aft plate. The leakage flow is simulated by additional outlet panels at the bar gap boundaries. The blade passage is discretized using an OCGH-topology and low-Reynolds wall treatment (non-dimensional wall distance $y+ \leq 1$), resulting in high boundary layer resolution. Sufficient spatial and temporal discretization is ensured by a sensitivity study, which leads

to an overall number of nodes of approximately 8×10^6 and a blade o-grid with 354, 31, and 110 nodes in the i,j,k-directions, respectively. The CFL number is set to 150 in the unsteady simulations, and each moving domain period (two bar pitches) is resolved by 800 time steps. The flow conditions prescribed at the in- and outlet plane match the wind tunnel conditions in the experiment (M_{2th}, $Re_{2th} = f(T_{t1}, p_{t1}, p_3)$, and Tu_1). A detailed description of the computational approach can be found in [13].

The key flow characteristics inside the T106A blade passage are illustrated by means of CFD in Figure 2. Here, axial slices of the entropy generation rate and iso-surfaces of the Q-criterion (colored by streamwise vorticity indicating the sense of rotation) indicate loss production at midspan and the secondary flow region. In the 2D-flow region around midspan, the levels of loss production start off moderately in the predominately aft-loaded T106A. However, near the trailing edge (TE), strong adverse pressure gradients acting on the blade suction surface lead to the formation of a separation bubble. Under periodically unsteady inflow conditions, wake-induced transition periodically forces the suppression of the separation bubble. This unsteady effect is visible in the time-averaged flow in Figure 2 by a lack of alternating vorticity on the rear suction surface. Near the endwall, the formation of secondary flow as described e.g., by Sieverding [19] becomes apparent. When entering the blade passage, strong transverse pressure gradients caused by blade loading force the boundary layer fluid towards the suction surface. During this process, the flow is rolling up, is fed into the passage vortex and the merging horseshoe vortex pressure side leg, lifts off the endwall, and finally impinges on the blade suction surface. In addition to the resulting high losses, the secondary flow can be identified well by overturning close to the endwall and corresponding underturning at the upper edge of vortex interaction. In the case of unsteady inflow, the interaction of the wakes with the endwall boundary layer periodically delays the development of the passage vortex. This leads to the attenuation of the secondary flow further downstream and, hence, a reduction in the secondary losses. A more detailed analysis of the secondary vortex system can be found in [13] and the effect of blade loading is discussed in [6]. Furthermore, the interaction with the suction surface flow, which leads to the corner-vortex and counter-vortex is investigated in Part 2 [20].

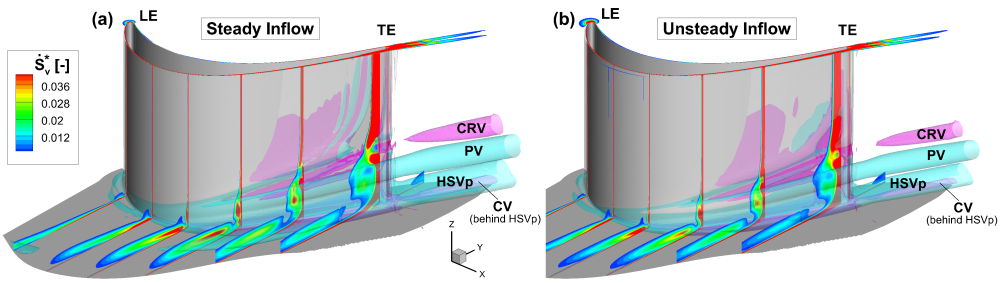

Figure 2. Simulated entropy generation rate ($\dot{S}_v^*$ non-dimensionalized) at several axial slices inside the T106A blade passage under steady (**a**) and periodically unsteady inflow conditions (**b**); adapted from Schubert et al. [13]; (HSVp—pressure side leg of horseshoe vortex; PV—passage vortex; CRV—counter-rotating vortex; CV—corner vortex; LE—leading edge; TE—trailing edge).

2.3. Experimental Setup

The experiments were conducted at the High-Speed Cascade Wind Tunnel (HGK) of the University of the Bundeswehr Munich, see Niehuis and Bitter [21]. The facility allows aerothermodynamic investigations of turbomachinery components at engine-relevant Mach and Reynolds numbers, which can be varied independently with respective uncertainties of 0.17% and 0.28%. For this reason, the main components of the HGK are enclosed by a large plenum chamber with a 4 m diameter and a 12 m length. The absolute pressure in this plenum chamber can be evacuated down to 4 kPa or pressurized up to 1.2 MPa. The wide pressure range together with the large test section dimensions make it possible to perform aerodynamic investigations on relatively large test specimens, even for low operating Reynolds numbers. This mitigates the relative influence of probe-based measurement

techniques on the flow field, especially at the high downstream Mach numbers typically encountered on a turbine cascade [22]. The HGK's test section can be equipped with a wake generator that produces periodically incoming wakes of up to around 500 Hz at the cascade inlet, see Acton and Fottner [23]. The periodically incoming wakes are generated by steel bars with a diameter of 2 mm, i.e., 111% of the T106A trailing edge diameter. The moving bar plane, which runs parallel to the blade passage inlet plane, is located 86% C upstream of the blade leading edge. The ratio of bars to blade count is two-to-one, i.e., $P_b/P = 0.5$, and the bar speed is $V_b = 20\,\mathrm{m/s}$, which leads to a bar passing period of 2 ms (500 Hz). Previous experimental and numerical studies of the T106A turbine cascade have shown that increased bar velocity (higher Strouhal number Sr and lower flow coefficient Φ) results in intensified effects on the secondary flow, see Ciorciari et al. [5]. However, within a reasonable range of unsteady inflow parameters, the observed trends remain unchanged.

The goal of the experiments was to measure an extensive flow field close to the endwall inside and downstream of the blade passage and demonstrate the time-dependent behavior with respect to the periodic bar wake effects. Therefore, two separate measurement setups using particle image velocimetry (PIV) were applied. Measuring a highly resolved passage flow field under high-speed conditions in close vicinity to a parallel wall and under severe vibrations of the wake generator was extremely challenging. In the first setup, the design of the test specimen and the blade-to-blade measurement plane required optical access to the flow passage through several side walls (see Figure 3a,b). Therefore, a single sCMOS camera with 5.5 Mpx resolution was connected to a 35 mm optical lens and a 220 mm long rod endoscope with an 8 mm diameter and 67° opening angle. The optical access into the passage from the opposite endwall is shown in Figure 3c. A light sheet generated by an Innolas Spitlight 1000 Nd:YAG laser with 480 mJ energy per pulse was introduced into the setup from downstream the cascade (see Figure 3d). As a consequence of the cambered blade passage, some areas were shadowed, and data evaluation was impeded. A calibration plate (see Figure 3e) with 2 mm dots arranged with 10 mm constant spacing was specifically tailored to the blade passage to calibrate the 2D2C-PIV images and compensate for the image distortions resulting from the non-ideal optical path through the endoscope. Two planes at $z = 65.5\,\mathrm{mm}$ ($z/H = 0.5$) and $z = 26.2\,\mathrm{mm}$ ($z/H = 0.2$) were investigated, and are named 'midspan' and 'near-wall' later in the text. The second—in this case, stereoscopic (or 2D3C) PIV setup, which delivers three velocity vector components—aims to resolve axial measurement plane 2 (MP 2) located 40% C_x downstream of the blade trailing edge (see Figure 4a). As depicted in Figure 4b, the setup featured two sCMOS cameras, and due to limited optical accessibility, the measurement plane had to be captured via two camera mirrors. The axial light sheet was formed at the bottom of the cascade and guided into the measurement as shown in Figure 4a,c. DEHS oil droplets with a mean diameter of 0.9 µm were used as seeding particles. This type of tracer particle ensures sufficient dynamic response to the flow at low static pressures, see Humble et al. [24] and Bitter et al. [25]. For each measurement, a set of 10,000 PIV images was processed by a 48-by-48 px cross-correlation with 50% overlap and a magnification factor of 1/10, leading to a resolution of 5 mm per velocity vector.

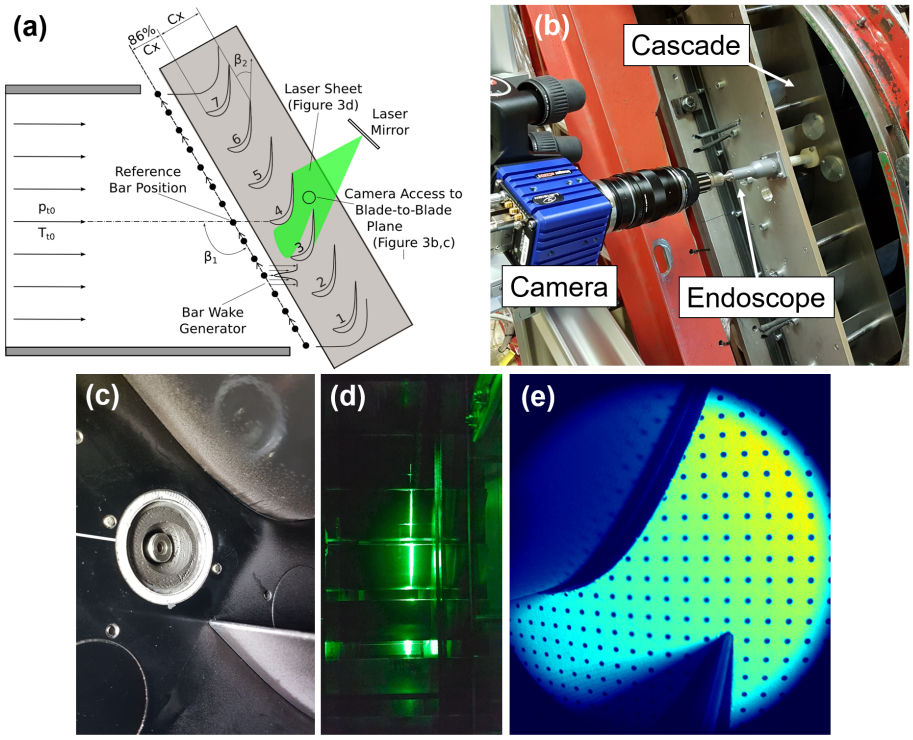

Figure 3. The 2D2C PIV setup for blade-to-blade measurements inside the T106A linear cascade; (**a**) schematic of the cross-sectional side view; (**b**) endoscopic camera setup; (**c**) optical access into the flow channel; (**d**) PIV laser sheet at $z/H = 0.2$; (**e**) camera calibration target in the field of view.

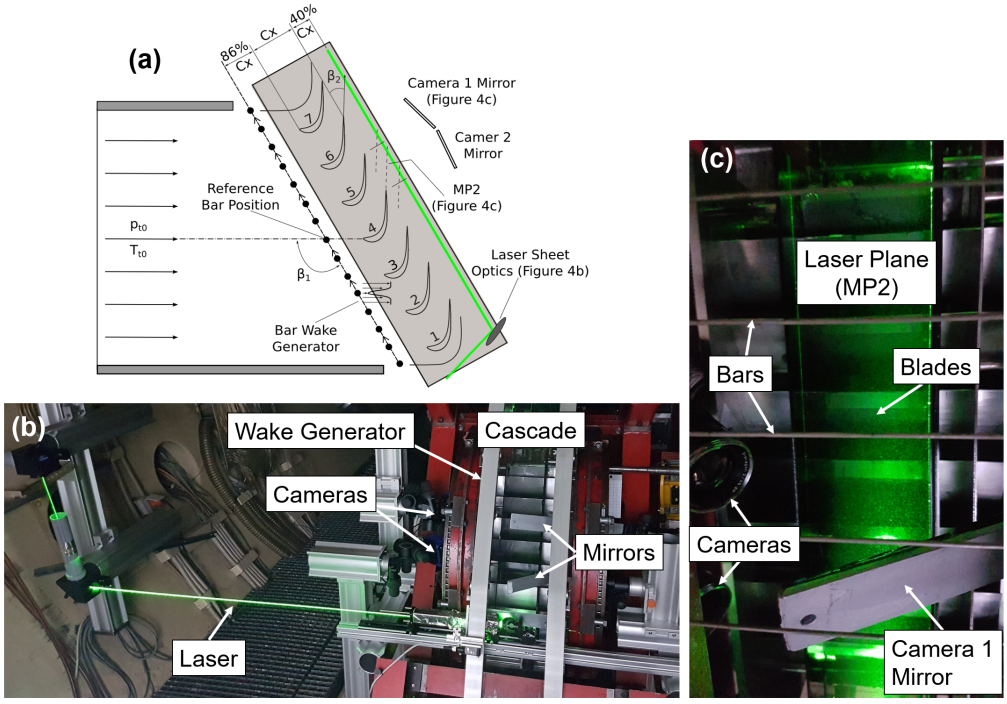

Figure 4. PIV setup for 2D3C measurements in an axial plane (MP 2) located 40% C_x downstream of the blade passage; (**a**) schematic of the cross-sectional side view; (**b**) camera setup and laser guidance to the test section; (**c**) laser sheet in the cascade exit flow.

A phase-averaging method according to Bitter and Niehuis [26] was performed in both PIV setups whereby all velocity fields were related to the bar reference position outlined

in Figure 5. The recording of both the camera trigger timing and the bar position signals at more than 1 MHz ensured precise sorting of all images and enabled a time-dependent discussion of the periodic wake effects in both PIV measurements, which were performed subsequently. The image sets were recorded at 15.1 Hz, while the dominant bar passing frequency was 502 Hz. The data had to be synchronized in post-processing by establishing a correlation between the geometric bar position y_b and the temporal bar period t_{BP}. The first step is to define a reference bar position. In the experimental setup, a bar was aligned with the leading edge of the measurement blade by placing a steel ruler on top and leveling it (see Figure 5a). This reference bar position was then identified by measuring the current pitchwise distance $\Delta y_{b,ref}$ to the next trigger point of an optical sensor, which registers each passing bar (see Figure 5b,c). Finally a timestamp τ was assigned for each measurement point by determining the relative time difference to the next bar trigger (see Figure 5d)

$$\frac{\tau}{t_{BP}} = \frac{t}{t_{BP}} - \frac{\Delta y_{b,ref}}{P_b}. \tag{1}$$

In addition to synchronization, the measured data were binned and subsequently averaged according to their position within the bar passing period τ/t_{BP}. As seen in Figure 5e, this method led to a statistically uniform distribution of measurement points per τ-bin. This sorting method can be adjusted on demand. The more bins that are chosen, the higher the temporal resolution of the bar wake passing through the passage but the lower the number of PIV images per bin for averaging the flow field. For the following discussions, 20 bins were chosen that included about 470 frames each. The synchronization process was also applied to the CFD data by determining the reference bar position and setting the correlating timestamp to zero (see Figure 5f).

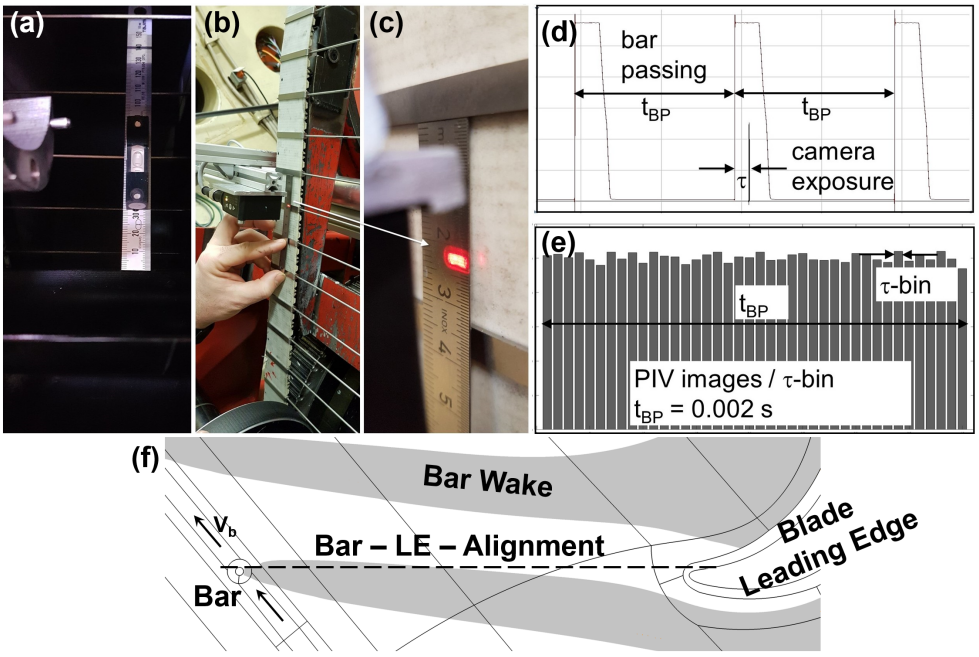

Figure 5. Phase-locking and synchronization method; (**a**–**c**) alignment of the spatial bar position with the temporal trigger signals of the bar counter; (**d**) assignment of a timestamp τ based on the relative position during a bar passing period; (**e**) binning and subsequent averaging in τ-bins of 0.1 ms; (**f**) application of the synchronization process to CFD by setting the reference bar position to $\tau = 0$.

3. Results

3.1. Time-Averaged Flow Fields

The mean Mach number distributions averaged over all 10,000 PIV vector fields are compared to five-hole-probe (FHP) measurements (performed in [8]) and to CFD in Figure 6. The upper row shows the axial exit flow fields under steady conditions (no bar wakes) and the lower row highlights the mean flow with incoming wakes. The results from both experimental techniques exhibit a good match in terms of flow topology and absolute values, which validates the presented PIV setup. Only at z/H = 0.2, where the pitchwise-averaged loss peak is located, are the interacting passage vortex (PV) and the counter-rotating vortex (CRV) slightly less distinct in the PIV measurements. The unsteady inflow conditions created by periodically incoming wakes lead to secondary flow attenuation, which is equally apparent in both data sets. The following discussion of the phase-locked PIV data in Section 3.2, including additional flow properties such as turbulent kinetic energy, will highlight the added benefit and the potential of the presented optical measurements as a supplement to the classic probe-based approach. The validated CFD setup [13] predicts a narrower but more intense blade wake and secondary flow in the downstream flow field. This is a well-documented characteristic of RANS-based flow simulations with eddy-viscosity modeling. However, the important value of overall integral losses (ζ_{FHP}= 4.7%, ζ_{CFD} = 4.6%) as well as the effect of periodically incoming wakes show a good match with the measurements.

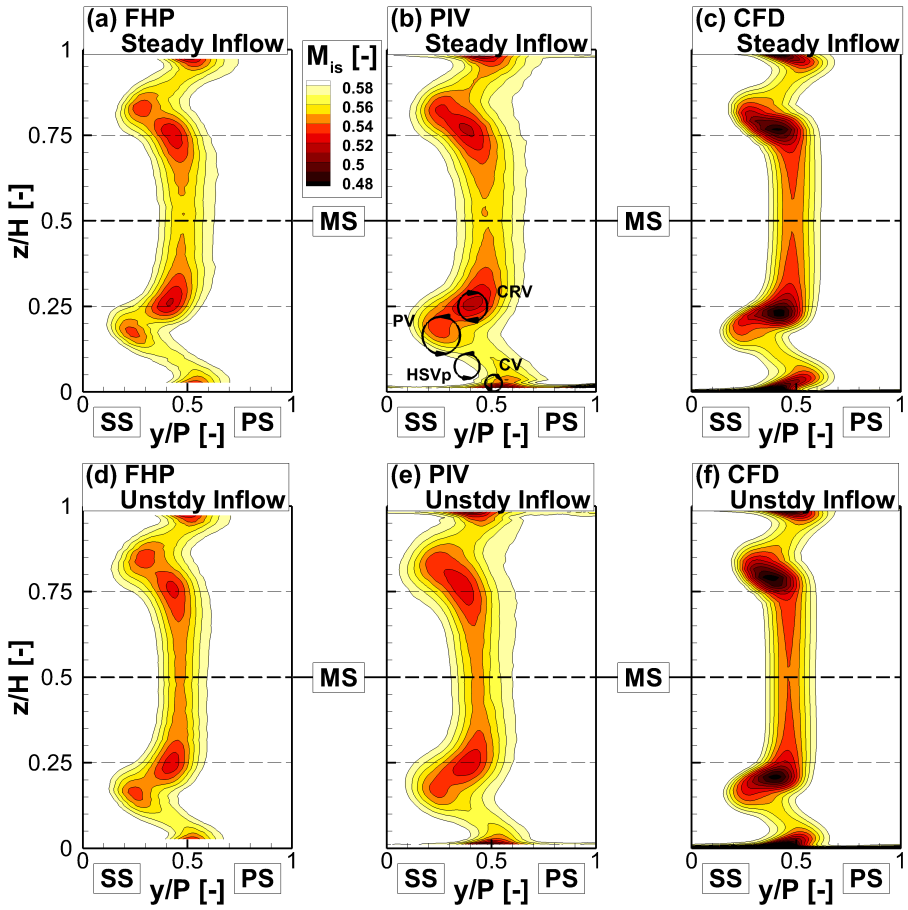

Figure 6. Time-averaged velocity distributions illustrated by isentropic Mach number in the downstream flow field (MP 2) under steady (**a**–**c**) and periodically unsteady inflow conditions (**d**–**f**).

In Figure 7, time-averaged blade-to-blade flow fields measured near the endwall at z/H = 0.2 are shown under steady and periodically unsteady inflow conditions. The velocity values in the left and center plots were ensemble-averaged over the entire image

series and normalized by the theoretic exit velocity of V_{2th} = 195.8 m/s at M_{2th} = 0.59. On the right, the time-averaged effect of the periodically incoming wakes is highlighted by the absolute velocity difference (blue—positive; red—negative). Throughout the passage flow field, the absolute velocity is slightly lower under periodically unsteady inflow conditions, resulting in a negative delta. The effect is strongest in the blade wake, leading to a higher time-averaged velocity deficit. The measured mean inlet velocity loss matches well with previous analytical calculations and CTA measurements by Schubert et al. [8], validating the PIV setup in the blade-to-blade plane. In a rotating turbine with multiple blade rows, the inlet losses close to the endwall will likely be even higher because the incoming wakes are superimposed with upstream secondary flows. In the white areas, especially close to the suction surface of the upper blade, data availability is limited due to the strong background illumination caused by direct laser reflections. Unfortunately, in this region, the secondary vortex system is partially formed and interacts with the blade profile flow, as seen in Figure 2. However, downstream of the trailing edge, a blue area is apparent on the suction side of the blade wake, which leads to the position on the passage vortex core in MP 2 (see *P*3 in Figure 7). This positive velocity delta illustrates a reduction in the velocity deficit due to vortex dissipation and thus implies attenuation of the secondary flow.

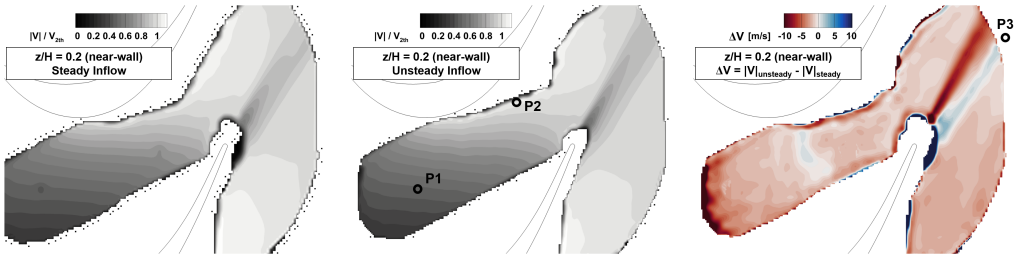

Figure 7. Time-averaged passage flow field at z/H = 0.2 (near-endwall) under steady (**left**) and periodically unsteady (**middle**) inflow conditions; (**right**) $\Delta|V|$ between the two cases of inflow conditions.

An alternative way to quantify the time-averaged secondary flow attenuation by the incoming wakes is by measuring the flow angle perturbation, as illustrated in Figure 8. The reference FHP measurements on the right side of Figure 8 illustrate the spanwise distribution of the pitchwise-averaged secondary outflow angle $\Delta\beta_{sec}$ in the axial plane MP 2 [8]. It is apparent that the vortex motion of the secondary flow, which is mainly driven by the dominant passage vortex, causes overturning in the nearest proximity of the endwall, followed by a region of underturning. Thus, the level of over-/underturning is a gauge of the secondary flow intensity. The 'near-wall' blade-to-blade plane of the PIV measurements was chosen to be located at the peak of the pitchwise-averaged underturning (z/H = 0.2). Since the secondary flow angle is calculated by subtracting the midspan flow field, the two visible passage flow fields in Figure 8 are reduced in size. This is a consequence of the 67° opening angle of the camera endoscope. It is apparent that the positive flow angle difference, i.e., underturning, starts slightly downstream of the midpoint of the passage ($x/C_x \approx 0.6$) as a reaction to the strong transverse pressure gradients, which force the initial overturning in the endwall boundary layer. Under periodically unsteady inflow conditions, the level of underturning is reduced inside the passage and in the downstream flow field. The PIV data indicate the same quantifiable trend as the probe measurements but in a much larger and less accessible measurement field. In addition to the secondary losses associated with the dissipation of the vortices, aerodynamic performance suffers from high over-/underturning since the downstream blade rows experience severe off-design conditions. Hence, endwall flow effects such as over-/underturning must be considered in the design of a turbomachinery stage.

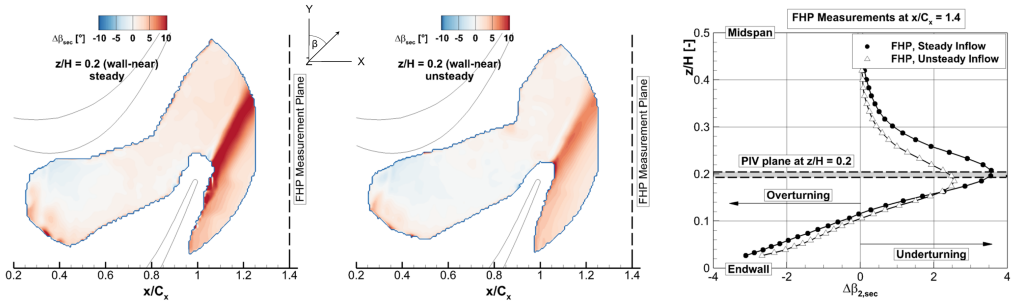

Figure 8. Time-averaged flow angle difference with respect to midspan at $z/H = 0.2$ ($\Delta\beta_{sec} = \beta - \bar{\beta}_{MS}$) under steady (**left**) and periodically unsteady (**middle**) inflow conditions; (**right**) $\Delta\beta_{sec}$ measured with a five-hole-probe at $x/C_x = 1.4$ downstream of the cascade.

3.2. Phase-Locked Flow Fields

Figure 9 shows the temporal behavior of the passage flow field near the endwall ($z/H = 0.2$) at four time steps τ of one bar passing period t_{BP}. The normalized absolute velocity fluctuation is given by $|V|'/V_{2th} = (|\bar{V}|(\tau) - \langle|V|\rangle)/V_{2th}$, where $|\bar{V}|(\tau)$ is the mean absolute velocity of a τ-bin, $\langle|V|\rangle$ is the ensemble average over the entire time series, and V_{2th} is the theoretical turbine exit velocity. The data were averaged for 20 time steps per period, resulting in around 470 PIV images per τ-bin. The flow field exhibits alternating positive and negative velocity fluctuations with an amplitude of about 3.5% in the front part of the passage. The relative velocity deficit of the wake is indicated by blue color. The streamline deformation of the wake passing through the passage is evident. The biggest contributors to the stretching and bowing are the strong acceleration near the pressure surface and the transverse pressure gradients towards the suction surface. Aided by the relatively low flow coefficient of the present periodic inflow, the wakes are almost parallel to the blade profile at around the passage throat. As the freestream mixing of the bar wakes accumulates in the flow direction, the measured wakes become less distinct, and the levels of velocity fluctuations continually decrease. For data synchronization, $\tau/t_{BP} = 0$ was defined by one random bar being located upstream in the design inflow direction of the reference blade leading edge. Based on the inflow velocity triangles of the moving bars, the wake reaches the leading edge of the blade slightly later in time. The corresponding phase lag between the bar position and the wake entry into the passage was calculated to be about $-45°$. Also, indicated in Figure 9 by arrowheads is every eighth velocity vector. This illustrates the relative flow direction and highlights the 'negative-jet-effect' of the bar wakes. This effect, which is indicated by blue color and reverse arrowheads (lower right to upper left), is a typical phenomenon in multistage turbomachinery as a consequence of the rotor–stator interaction. It was comprehensively studied by Hodson et al. [27]. In the present case, the flow vectors clearly show an alternating relative flow angle β'. The negative jet imposes relative fluid transport towards the suction surface. Where the negative jet impinges on the blade suction surface, it is periodically inducing a local positive pressure gradient on the boundary layer, which is prone to flow separation, especially downstream of the passage throat due to high loading and decelerating flow. In addition to the mean velocity deficit, the cylindrical bar wakes produce a turbulence intensity increase of around 20% in their cores [26]. Further downstream, these levels are mixed with the main flow inlet turbulence intensity of about 6.8%. The resulting periodic increase in turbulence triggers an earlier suction surface boundary layer transition (wake-induced transition), which increases the robustness against flow separation. The overall effect of the negative jet on the blade suction surface flow will be discussed in more detail in the second part of this two-part publication using high-speed pressure-sensitive paint measurements.

A comparison of the velocity fluctuations and the passage flow angles between the experiments and the numerical simulations is performed in Figure 10. The data for the time plot were extracted at location $P1$ ($x/C_x = 0.3$), which is marked in Figure 7. Good correlation for both phase and amplitude between experiments and CFD is evident. The

lower peak amplitudes of around 3%-points for the measured data is partially due to the fact that the CFD data are exported at a higher number of 80 time steps per period, while the measured fluctuations are phase averaged in 20 τ-bins.

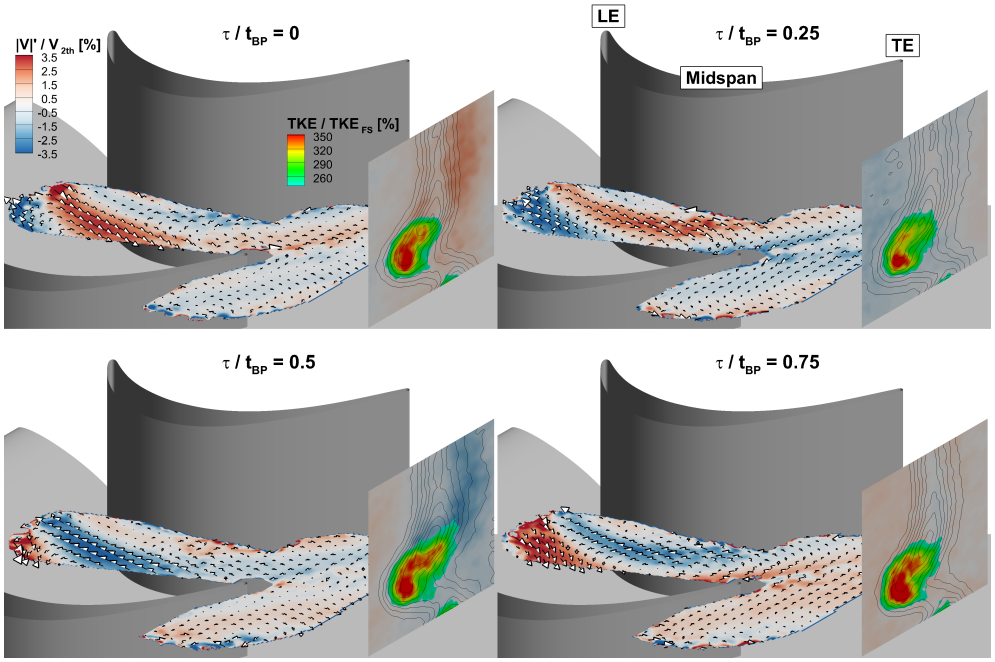

Figure 9. Transport of the bar wake velocity deficit through the T106A turbine passage close to the endwall (z/H = 0.2) at four time steps and its effect on the downstream flow field.

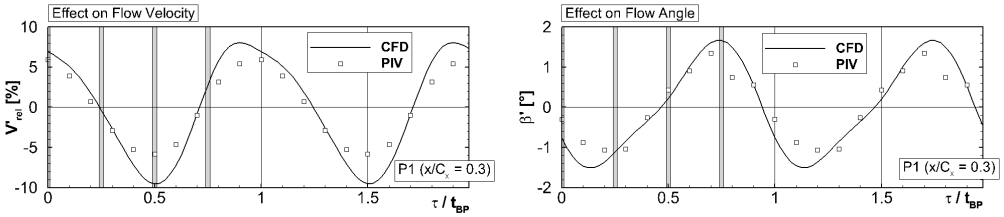

Figure 10. Evolution of the bar wake effect on the near-endwall (z/H = 0.2) passage flow field at position $P1$ (see Figure 10) over time; comparison of velocity deficit and the flow angle between CFD and phase-locked PIV (gray positions in the time plot mark the displays in Figure 9).

Next to the PIV blade-to-blade plane, Figure 9 also includes the PIV measurements in the downstream flow field. The transport of the bar wakes is clearly traceable all throughout the blade passage into the downstream axial plane (MP 2), which illustrates the quality of the two isolated measurements and the applied synchronization method. The additional black velocity contour lines and turbulent kinetic energy enables the relation between the sequence of the moving bar wakes and their effects on the downstream flow field. There are two major indicators by which these effects were evaluated: the pitchwise extension of the secondary flow field and the intensity of the vortex interaction. As the bar wake travels from left to right through the axial plane, it overlaps with the secondary flow field on the suction side of the blade. During this process, the extension of the secondary flow field remains relatively stable. However, the width of the blade wake is significantly increased, especially on the pressure side of the blade (τ/t_{BP} = 0.25 and 0.5). On the other hand, when the bar wake is out of the frame in MP 2, the blade wake is significantly narrower (τ/t_{BP} = 0 and 0.75). In order to better quantify these effects, the flow velocity iso-line value of $|V|/V_{2th}$ = 95% was defined as the boundary of the secondary flow field and the blade wake. Its position was then measured on the suction side and pressure side in each time step. The resulting periodic shift at z/H = 0.2 relative to the time-averaged position

is shown in Figure 11a. The suction-side boundary is an indicator of the secondary flow extension, while the pressure-side boundary reflects the blade wake. Both assumptions are validated by confirming that the periodic sequences are in phase to key reference signals (see below). In all cases, positive values represent widening and negative values represent narrowing. The maximum blade wake extension is around three times higher than the maximum secondary flow extension. However, the most important finding here is not related to amplitudes but rather a phase lag of $-108°$, i.e., $\Delta\tau/t_{BP} = -0.3$ between the secondary flow extension and the blade wake extension. This phase lag is unique to the secondary flow and different from the behavior at midspan. Here, the start of the widening of the downstream blade wake corresponds to the overlap with the bar wake. As the bar wake passes through the axial plane, the suction- and pressure-side blade wake boundaries at midspan are affected simultaneously, i.e., $0°$ phase lag (see Figure 11b). This results in an increase in the wake width of up to 165%. All three midspan sequences are virtually in-phase ($18°$ phase lag) with the pressure-side extension at $z/H = 0.2$, proving it to be representative of the blade wake.

The secondary vortex intensity, as the second evaluation indicator, is measured by turbulent kinetic energy relative to the mean freestream TKE. It is apparent in Figure 9 that the TKE level increases as the bar wake passes through the secondary flow region ($\tau/t_{BP} = 0.25$ and 0.5). However, it continues to increase beyond the passing of the pressure side ($\tau/t_{BP} = 0.75$). Hence, the TKE evolution in the secondary flow region is not synchronized with the overlap of the bar wake in MP 2. In fact, the periodic change of averaged local TKE in Figure 11a exhibits the same phase lag of $-108°$ to the bar wake passing as the secondary flow extension. However, for the secondary flow intensity, it is the low levels of TKE that are associated with the bar wake effects. Therefore, both signals are in sync even though they appear to have a $180°$ lag. This means the lowest intensity correlates to the highest pitchwise extension, or in other words, at that moment, the secondary vortices are less distinct due to a higher degree of mixing.

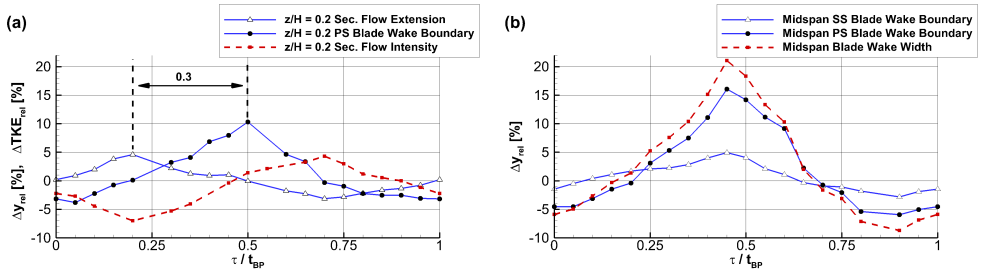

Figure 11. Periodic effect of the bar wakes on the downstream flow field (MP 2); (**a**) secondary flow extension $\Delta y_{rel} = (y - \langle y \rangle)/P$ and intensity $\Delta TKE_{rel} = (TKE - \langle TKE \rangle)/\langle TKE \rangle$ at $z/H = 0.2$; (**b**) blade wake extension Δy_{rel} at midspan.

Overall, these findings indicate that the fully developed secondary flow downstream of the blade passage is highly resistant to a direct perturbation due to overlapping with the bar wakes. Instead, the observed periodic changes in secondary flow extension and intensity is caused further upstream. Starting from the passage vortex core position in MP 2 (see *P*3 in Figure 7), the mean origin of these effects can be calculated based on the identified phase lag of ($\Delta\tau/t_{BP} = -0.3$ i.e., -0.6 ms) and the measured blade-to-blade velocity field. It is located inside the blade passage at $x/C_x = 0.72$ (see *P*2 in Figure 7). Around this location, endwall boundary layer fluid that has been driven towards the suction surface is about to be detached, rolled up, and fed into the passage vortex. The perturbation of this process by wake interaction and the consequent secondary flow attenuation was previously investigated using numerical simulations of the present test case in [13].

4. Conclusions

An experimental campaign was conducted using a T106A linear turbine cascade with an additional part-span endwall under challenging measurement conditions with periodically incoming wakes with a frequency of 500 Hz. In previous investigations, the authors utilized a combination of probe-based measurements and CFD to identify attenuation of the downstream secondary flow caused by wake interaction inside the blade passage. The primary goal of the experiments presented here was to validate, complement, and specify these findings. This was achieved by implementing and synchronizing two isolated phase-locked PIV measurement setups in a blade-to-blade plane close to the endwall and an axial plane downstream of the passage. Classic downstream five-hole-probe flow angle measurements were extended by combining PIV distributions at midspan and close to the endwall to quantify the change in over-/underturning caused by the wakes throughout the passage. Wake stretching and bowing could be traced throughout the blade passage and beyond. In this context, the 'negative-jet-effect' could clearly be illustrated, and supporting CFD showed a good match in phase and amplitude. In the downstream flow field, the bar wakes periodically increased the width of the blade wake by up to 165%. The fully developed secondary flow, on the other hand, was highly resistant to a direct perturbation by overlapping bar wakes. The periodic increase in secondary flow extension and in-phase decrease in turbulent kinetic energy exhibited a phase lag of $-108°$, i.e., $\Delta\tau/t_{BP} = -0.3$ to the bar wake overlap. It was concluded that the secondary flow attenuation is caused further upstream by wake interaction with the endwall boundary layer and, hence, the vortex formation. By combining the identified phase lag and the measured blade-to-blade velocity field, the mean origin of this effect was located inside the blade passage at around $x/C_x = 0.72$. Overall, it has been demonstrated that, particularly for secondary flow investigations under periodic inflow conditions, optical measurements such as phase-locked PIV provide a valuable addition to classic probe-based measurement approaches.

The results presented here are an essential basis for the subsequent investigation of the near-endwall blade suction surface effects in the second part of this two-part publication. A preview of the comprehensive experimental data set comprising periodically unsteady suction surface pressure fields is given in Figure 12. The surface data were measured with unsteady pressure-sensitive paint (i-PSP). The i-PSP measurements were performed using the intensity method, high-power uv-LED excitation, and a high-speed camera sampled at 30 kHz. Single- to double-digit Pascal pressure amplitudes could be resolved precisely and correlate well with CFD. Furthermore, two frequency filtering methods were compared to identify distinct flow features in the frequency spectrum up to several kilohertz.

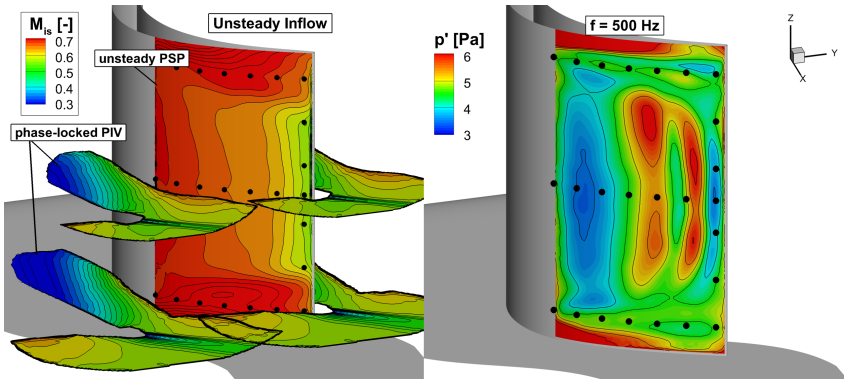

Figure 12. Illustration of the experimental data set available for the T106A test case under unsteady inflow conditions; (**left**) duplicated PIV passage flow fields presented in this paper and time-averaged isentropic surface Mach number on the blade suction surface measured with unsteady pressure-sensitive paint; (**right**) high-resolution surface pressure amplitude measurement (PSP) stimulated by the dominant wake generator frequency around 500 Hz. Black dots show markers for image mapping.

Author Contributions: Conceptualization, T.S. and M.B.; Methodology, T.S. and M.B.; Software, T.S.; Validation, T.S.; Formal analysis, T.S.; Investigation, T.S.; Resources, D.K.; Data curation, T.S.; Writing—original draft, T.S.; Writing—review & editing, T.S. and M.B.; Visualization, T.S.; Supervision, D.K. and M.B.; Project administration, T.S. and M.B.; Funding acquisition, T.S. and M.B. All authors have read and agreed to the published version of the manuscript.

Funding: The numerical design as well as the experimental investigations presented in this paper were performed in the framework of the joint project PAK 948 'Flow near the endwall of turbomachinery blading' funded by Deutsche Forschungsgemeinschaft under funding code Ma 4922/8-1.

Data Availability Statement: The raw data supporting the conclusions of this article will be made available by the authors on request.

Conflicts of Interest: The authors declare no conflicts of interest.

Nomenclature

Latin symbols	
C	chord length
H	channel height, i.e., blade span
H_{12}	boundary layer shape factor
M	Mach number
p	pressure
P	pitch
Re	Reynolds number
$\dot{S}_v^*$	non-dimensional entropy generation rate per unit volume, $\dot{S}_v \times (C \times T_{2,th})/(\rho_{2,th} \times V_{2,th})$
Sr	Strouhal number, $(V_b/P_b) \times (C/V_{x1})$
T	temperature
Tu	turbulence intensity
t	time
V	velocity
V'	velocity fluctuation
$\|V\|$	absolute velocity
$\langle V \rangle$	ensemble averaged velocity
x, y, z	axial, pitchwise, and spanwise coordinates
Greek symbols	
β	flow pitch angle
δ_{99}	boundary layer thickness
ϕ	flow coefficient, V_{x1}/V_b
τ	synchronized timestamp
ζ	total pressure loss coefficient
Abbreviations	
CV	corner vortex
CRV	counter-rotating vortex
DEHS	Di-Ethyl-Hexyl-Sebacat
EW	endwall
FHP	five-hole-probe
FS	freestream
HSVp	horseshoe vortex pressure side leg
i-PSP	unsteady pressure-sensitive paint
Laser	light amplification by stimulated emission of radiation
MP 2	measurement plane 2, 40% C_x downstream TE
MS	midspan
PV	passage vortex
sCMOS	scientific complementary metal–oxide–semiconductor
Subscripts	
1	inflow condition
2	downstream measurement plane

b	bar
BP	bar passing
t	stagnation quantity
sec	secondary

References

1. Cui, J.; Tucker, P.G. Numerical Study of Purge and Secondary Flows in a Low Pressure Turbine. In Proceedings of the ASME Turbo Expo 2016: Turbomachinery Technical Conference and Exposition, Seoul, Republic of Korea, 13–17 June 2016; ASME GT2016-56789.
2. Coull, J.D. Enwall Loss in Turbine Cascades. *J. Turbomach.* **2017**, *139*, 081004. [CrossRef]
3. Denton, J.; Pullan, G. A Numerical Investigation into the Sources of Endwall Loss in Axial Flow Turbines. In Proceedings of the ASME Turbo Expo 2012: Turbine Technical Conference and Exposition, Copenhagen, Denmark, 11–15 June 2012; ASME GT2012-69173.
4. Bear, P.; Wolff, M.; Gross, A.; Marks, C.R.; Sondergaard, R. Experimental Investigation of Total Pressure Loss Development in a Highly Loaded Low-Pressure Turbine Cascade. *J. Turbomach.* **2018**, *140*, 031003. [CrossRef]
5. Ciorciari, R.; Kirik, I.; Niehuis, R. Effects of Unsteady Wakes on Secondary Flows in the Linear T106 Turbine Cascade. *J. Turbomach.* **2014**, *136*, 091010. [CrossRef]
6. Ciorciari, R.; Schubert, T.; Niehuis, R. Numerical Investigation of Secondary Flow and Loss Development in a Low Pressure Tubrine Cascade with Divergent Endwalls. *Int. J. Turbomach. Propuls. Power* **2018**, *3*, 5. [CrossRef]
7. Volino, R. Effects on Endwall Boundary Layer Thickness and Blade Tip Geometry on Flow through High Pressure Turbine Passages. In Proceedings of the ASME Turbo Expo 2014: Turbine Technical Conference and Exposition, Düsseldorf, Germany, 16–20 June 2014; ASME GT2014-27013.
8. Schubert, T.; Chemnitz, S.; Niehuis, R. The Effects of Inlet Boundary Layer Condition and Periodically Incoming Wakes on Secondary Flow in a Low Pressure Turbine Cascade. *J. Turbomach.* **2021**, *143*: 041001. [CrossRef]
9. Sinkwitz, M.; Winhart, B.; Engelmann, D.; di Mare, F. Time-Resolved Measurements of the Unsteady Boundary Layer in an Annular Low-Pressure Turbine Configuration With Perturbed Inlet. *J. Turbomach.* **2021**, *144*, 011001. [CrossRef]
10. Lopes, G.; Simonassi, L.; Lavagnoli, S. Impact of Unsteady Wakes on the Secondary Flows of a High-Speed Low-Pressure Turbine Cascade. *Int. J. Turbomach. Propuls. Power* **2023**, *8*, 36. [CrossRef]
11. Chemnitz, S.; Niehuis, R. A Comparison of Turbulence Levels from Particle Image Velocimetry and Constant Temperature Anemometry Downstream of a Low-Pressure Turbine Cascade at High-Speed Flow Conditions. *J. Turbomach.* **2020**, *142*, 071008. [CrossRef]
12. Engelmann, D.; Sinkwitz, M.; di Mare, F.; Koppe, B.; Mailach, R.; Ventosa-Molina, J.; Fröhlich, J.; Schubert, T.; Niehuis, R. Near-Wall Flow in Turbomachinery Cascades—Results of a German Collaborative Project. *J. Turbomach. Propuls. Power* **2021**, *6*, 9.
13. Schubert, T.; Niehuis, R. Numerical Investigation of Loss Development in a Low-Pressure Turbine Cascade with Unsteady Inflow and Varying Inlet Endwall Boundary Layer. In Proceedings of the ASME Turbo Expo 2021: Turbomachinery Technical Conference and Exposition, Virtual, 7–11 June 2021; ASME GT2021-59696.
14. Kampitsch, M.; Stadtmüller, P.; Fottner, L. Investigations of Wake-Induced Transition on the LPT Cascades T106A-EIZ and T106D-EIZ. In Proceedings of the ERCOFTAC Workshop, La Clusaz, France, 19–23 March 2000.
15. Kirik, I.; Niehuis, R. Comparing the Effect of Unsteady Wakes on Parallel and Divergent Endwalls in a LP Turbine Cascade. In Proceedings of the 11th International Gas Turbine Congress, Tokyo, Japan, 15–20 November 2015; IGTC2015-137.
16. Michelassi, V.; Chen, L.; Pichler, R.; Sandberg, R.D. Compressible Direct Numerical Simulation of Low-Pressure Turbines—Part II: Effect of Inflow Disturbances. *J. Turbomach.* **2015**, *137*, 071005. [CrossRef]
17. Wilcox, D.C. *Turbulence Modeling for CFD*, 4th ed.; DCW Industries: La Canada, CA, USA, 2004.
18. Langtry, R.B.; Menter, F.R. Transition Modeling for General CFD Applications in Aeronautics. In Proceedings of the 43rd AIAA Aerospace Sciences Meeting and Exhibit, Reno, NV, USA, 10–13 January 2005; AIAA Paper 2005-522.
19. Sieverding, C. Recent Progress in the Understanding of Basic Aspects of Secondary Flows in Turbine Blade Passages; *ASME J. Eng. Gas Turbines Power.* **1985**, *107*, 248–257. [CrossRef]
20. Schubert, T.; Kožulović, D.; Bitter, M. Characterization of the Endwall Flow in a Low-Pressure Turbine Cascade Perturbed by Periodically Incoming Wakes. Part 2: Unsteady Blade Surface Measurements Using Pressure-Sensitive Paint. *Aerospace* **2024**, *11*, 404. [CrossRef]
21. Niehuis, R.; Bitter, M. The High-Speed Cascade Wind Tunnel at the Bundeswehr University Munich after a Major Revision and Upgrade. *Int. J. Turbomach. Propuls. Power* **2021**, *6*, 41. [CrossRef]
22. Börner, M.; Bitter, M.; Niehuis, R. On the Challenge of Five-Hole-Probe Measurements at High Subsonic Mach Numbers in the Wake of Transonic Turbine Cascades. *J. Global Power Propuls. Soc.* **2018**, *2*: 453–464. [CrossRef]
23. Acton, P.; Fottner, L. The Generation of Instationary Flow Conditions in the High-Speed Cascade Wind Tunnel of the German Armed Forces University Munich. In Proceedings of the 13th Symposium on Measuring Techniques, Zurich, Switzerland, 5–6 September 1996.

24. Humble, R.; Scarano, F.; Oudheusden, B.; Tuinstra, M. PIV Measurements of a Shock Wave/Turbulent Boundary Layer Interaction. In Proceedings of the 13th International Symposium on Applications of Laser Techniques to Fluid Mechanics, Lisbon, Portugal, 26–29 June 2006.
25. Bitter, M.; Kurz, J.; Kähler, C.; Niehuis, R. Investigations of a low-pressure turbine blade by means of simultaneous optical velocity and pressure measurements. In Proceedings of the 18th International Symposium on Applications of Laser Techniques to Fluid Mechanics, Lisbon, Portugal, 4–7 July 2016.
26. Bitter, M.; Niehuis, R. Effects of Periodic Inflow Turbulence on the Statistics in the Wake of a Linear LPT Cascade at Jet-Engine relevant Test Conditions. In Proceedings of the 13th International Symposium on Particle Image Velocimetry, Munich, Germany, 22–24 July 2019.
27. Hodson, H.P.; Hynes, T.P.; Greitzer, E.M.; Tan, C.S. A Physical Interpretation of Stagnation Pressure and Enthalpy Changes in Unsteady Flow. *J. Turbomach.* **2012**, *134*, 060902. [CrossRef]